Sparse Convolutional Beamforming for 3-D Ultrafast Ultrasound Imaging

Regev Cohen, *Student Member, IEEE*, Nitai Fingerhut, François Varray, *Member, IEEE*, Hervé Liebgott, and Yonina C. Eldar, *Fellow, IEEE*

***Abstract*— Real-time 3-D ultrasound (US) provides a complete visualization of inner body organs and blood vasculature, crucial for diagnosis and treatment of diverse diseases. However, 3-D systems require massive hardware due to the huge number of transducer elements and consequent data size. This increases cost significantly and limit both frame rate and image quality, thus preventing the 3-D US from being common practice in clinics worldwide. A recent study presented a technique called sparse convolutional beamforming algorithm (SCOBA), which obtains improved image quality while allowing notable element reduction in the context of 2-D focused imaging. In this article, we build upon previous work and introduce a nonlinear beamformer for 3-D imaging, called COBA-3D, consisting of 2-D spatial convolution of the in-phase and quadrature received signals. The proposed technique considers diverging-wave transmission and achieves improved image resolution and contrast compared with standard delay-and-sum beamforming while enabling a high frame rate. Incorporating 2-D sparse arrays into our method creates SCOBA-3D: a sparse beamformer that offers significant element reduction and, thus, allows performing 3-D imaging with the resources typically available for 2-D setups. To create 2-D thinned arrays, we present a scalable and systematic way to design 2-D fractal sparse arrays. The proposed framework paves the way for affordable ultrafast US devices that perform high-quality 3-D imaging, as demonstrated using phantom and ex-vivo data.**

***Index Terms*— 3-D imaging, array processing, beam pattern, beamforming, contrast, fractal arrays, medical ultrasound (US), resolution, sparse arrays.**

Manuscript received April 23, 2020; accepted March 16, 2021. Date of publication March 23, 2021; date of current version June 29, 2021. This work was supported in part by the LABEX PRIMES (ANR-10-LABX-0063) and was performed within the frameworks of LABEX CELYA (ANR-10-LABX-0060) of Université de Lyon, within the program "Investissements d'Avenir" (ANR-11-IDEX-0007) operated by the French National Research Agency (ANR), in part by the European Union's Horizon 2020 Research and Innovation Program under Grant 646804-ERC-COG-BNYQ, and in part by the Israel Science Foundation under Grant 0100101. *(Corresponding author: Regev Cohen.)*

Regev Cohen and Nitai Fingerhut are with the Department of Electrical Engineering, Technion–Israel Institute of Technology, Haifa 32000, Israel (e-mail: regev.cohen@gmail.com; nitaifingerhut@gmail.com).

François Varray and Hervé Liebgott are with the Department of Electrical Engineering, University of Lyon, INSA-Lyon, Université Claude Bernard Lyon 1, UJM-Saint Etienne, CNRS, Inserm, CREATIS UMR 5220, U1206, F-69621 Lyon, France.

Yonina C. Eldar is with the Faculty of Mathematics and Computer Science, Weizmann Institute of Science, Rehovot 7610001, Israel (e-mail: yonina.eldar@weizmann.ac.il).

Digital Object Identifier 10.1109/TUFFC.2021.3068078

I. Introduction

ULTRASONOGRAPHY is a prominent diagnosis technique, commonly used in clinical practices. The low-cost and radiation-free nature of ultrasound (US) imaging has facilitated its widespread use in medical applications, such as obstetrics, cardiology, and surgical guidance [1].

In standard 2-D US imaging, the image is created from multiple scan-lines. Transducer elements are used to sequentially transmit short acoustic pulses into the medium, focused in different directions. The acoustic signals are reflected back due to tissue perturbations and are received by the array elements. Upon reception, the signals are sampled and digitally beamformed to yield a line in the image. This process is repeated in consecutive directions to create the complete image frame.

The performance of the above approach, used by most commercial US scanners, is characterized by the following major aspects: image quality (i.e., resolution and contrast), frame (or volume) rate, and processing rate. The common beamformer, delay-and-sum (DAS) [2], [3], is widely used due to its simplicity and real-time capabilities, but it suffers from poor resolution and contrast in certain setups, specifically in 3-D imaging. The number of transmit–receive sequences required to build all scan-lines is typically several hundreds in 2-D settings. This limits the frame rate to tens of frames per second, making it insufficient for cardiac applications, such as the proper evaluation of the fastest phenomena in the cardiovascular system (flow patterns in the aorta or pulse wave propagation) or shear wave elastography. A common approach to improve frame rate is the use of ultrafast imaging. Here, several tilted plane-waves or diverging-waves (DWs) are sequentially transmitted. Upon reception, a beamformed signal is created by DAS after each transmission, and the signals are then summed coherently to yield a final compounded image. This leads to a dramatic increase in frame rate while providing improved image resolution and contrast compared to commonly focused transmissions. However, since the entire region of interest is reconstructed following each transmission, this strategy increases the processing rate and exhibits a large computational load, which typically requires the use of graphics processing units [4].

Conventional 2-D US is highly operator-dependent as it relies on the physician's knowledge of the human anatomy and her or his expertise to comprehend 3-D anatomic structures

from several planar 2-D images. Performing 3-D imaging reduces operator dependence since, once the volumetric data are obtained, any arbitrary view of the data can be displayed, including anatomical structures within it, which are intrinsically 3-D. However, 3-D US necessitates the use of 2-D probes where the number of elements may reach several thousands. The latter implies a massive increase in the data size and processing rates, which may degrade frame rate and image quality. Furthermore, current 3-D imaging requires cumbersome hardware that is only available in a few research facilities (e.g., the parallelized Verasonics systems at the University of Lyon [5], the SARUS scanner at the Technical University of Denmark in Lyngby [6], the parallelized Aixplorer systems at the Langevin Institute in Paris [7]).

Due to the mentioned limitations, it is of utmost importance to develop efficient methods to perform high frame-rate 3-D imaging with limited hardware. This will enable the daily use of 3-D imaging in clinics worldwide.

Several techniques have been proposed that aim at reducing the large number of receive channels. Savord and Solomon [8] proposed a strategy called microbeamforming [8]–[18], where the array elements are divided to subarrays which are analog-beamformed. However, the latter requires custom expensive integrated circuits that exhibit high power consumption [8], [19], [20]. Moreover, the acquisition flexibility is reduced due to the predetermined delays associated with the subarrays. Chen *et al.* [21] proposed the use of 2-D row-column-addressed arrays [21]–[30], in which every row and column in the array acts as one large element. However, large elements may exhibit significant edge effects that limit image quality [22]. The notion of separable beamforming was introduced in [31] and [32], wherein 2-D beamforming is performed by two separable 1-D steps, which facilitates the computation but the overall amount of data remains the same.

Another approach, adopted from sonar processing, is synthetic aperture (SA) [8], [33]–[36], which performs channel multiplexing to address a full 2-D array with a small number of electronic channels. In this context, a method called multi-element synthetic transmit aperture (MSTA) was introduced in [37], where unfocused or DWs are transmitted using a limited number of active elements, while all the elements are utilized upon reception. In [38], SA was combined with short-lag spatial coherence. However, these techniques use all array elements on reception.

A promising framework for data reduction is compressed sensing (CS) [39], [40], which includes the concept of analog Xampling [41]–[51]. Such techniques focus on reducing the sampling rate by assuming that the US signal can be sparsely represented in some chosen basis. The reconstruction performance of US signals in different bases was investigated in [44]. A method for reducing the sampling rate was developed in [48] where the authors described the US echoes within the finite rate of innovation framework as a small number of replicas of a transmitted pulse [39], [40]. This approach was exploited to develop sub-Nyquist data acquisition [49], including plane-wave imaging [52] and volumetric imaging [53]. A different beamforming method, called CS-based synthetic transmit aperture [54], consists of transmitting a small number of randomly weighted plane-waves, thus increasing frame rate and using CS techniques for recovering the full channel data. Yet, none of the above considered receive element reduction.

An alternative interesting strategy is performing DAS beamforming with sparse arrays, where some of the elements are removed, including both random arrays and deterministic designs [55]–[63]. However, implementing DAS with random thinned arrays typically leads to increased average sidelobe levels. Given the desired number of active elements, 2-D sparse arrays can be optimized [59], [60], [64]–[66] to produce homogeneous imaging capability over the entire volume of interest. Still, such sparse arrays exhibit lower sensitivity compared to full arrays [67]. In addition, the array design is typically not scalable and has to be repeated for each setting.

Following the line of works on sparse arrays [55]–[63], [68]–[70], Cohen and Eldar [71] introduced a convolutional beamforming algorithm (COBA) based on the convolution of the delayed RF signals, which can be implemented at low complexity using the fast Fourier transform (FFT). COBA creates a virtual array, termed the sum coarray [69], which dictates the beamforming performance. For an appropriate element arrangement, the resultant sum coarray may be larger than the physical array, leading to a notable improvement in image resolution and contrast compared to standard DAS. Based on this, a sparse version of COBA can be used with a small number of elements, referred to as sparse COBA (SCOBA). SCOBA achieves a significant decrease in the number of elements without compromising image quality. COBA and SCOBA have been implemented in the context of 2-D imaging with the focused transmission; hence, they exhibit low frame rate and operator dependence characteristic of all 2-D methods.

In this work, we extend the notion of convolutional beamforming to 3-D imaging with DW transmission to allow ultrafast frame rate. We introduce a nonlinear beamformer, referred to as COBA-3D, which performs coherent compounding upon reception and then computes the 2-D spatial convolution of the resultant in-phase and quadrature (IQ) signals using 2-D FFT. We show that COBA-3D achieves improved 3-D image resolution and contrast in comparison to DAS. Incorporating 2-D sparse arrays into our framework leads to sparse COBA-3D (SCOBA-3D), which, in turn, provides significant element reduction, allowing us to perform high-quality 3-D imaging with the resources typically available in 2-D settings. Our approach relies on the design of 2-D sparse arrays that pose an engineering challenge. To address this, we present a simple scheme for constructing arbitrarily large 2-D fractal arrays [72]–[78] on which SCOBA-3D can operate.

We validate the proposed methods using phantom scans that include point reflectors and anechoic cysts to assess image resolution and contrast. We qualitatively and quantitatively show that COBA-3D outperforms standard DAS with coherent compounding. Results obtained by SCOBA-3D prove that we can utilize an order-of-magnitude lower number of receive elements, reduced from 961 elements composing the full array to just 169 ($\approx$ 18%), without compromising image quality. To strengthen our results, we show images obtained

from *ex vivo* data, setting the path toward real-time clinical application of the proposed methods.

The rest of this article is organized as follows. In Section II, we derive an expression for the 2-D beam pattern and formulate our problem. Section III describes the convolutional beamformer for 3-D imaging with DWs' transmission. We further describe the use of sparse arrays to obtain element reduction and present our fractal array design. In Section IV, we evaluate the performance of our beamformers in different settings using phantom and *ex-vivo* data. Finally, Section V concludes this article.

II. Beam Pattern and Problem Description

A. Beam Pattern

We begin by presenting the concept of a 2-D US beam pattern that provides a mean for the design and evaluation of beamformers, as well as the transducer arrays on which they operate. The following presentation is based on [71], extended to the 3-D setting.

Consider a 2-D uniform planar array (UPA) whose sensors are located in the xy-plane at

$$p_{n,m} = (nd_x, md_y, 0), \quad n \in [-N, N], \ m \in [-M, M] \tag{1}$$

where $N, M \in \mathbb{N}^+$, d_x and d_y are the element spacing (pitch) in the x- and y-directions, respectively, and z represents the axial axis.

At the reception, consider a scatterer located at (r, θ, ϕ), where r is the distance from the center of the array, and θ and ϕ are the azimuth and elevation angles, respectively. An acoustic pulse is reflected off the scatterer and propagates back through the tissue at the speed of sound c, assumed to be constant. The backscattered signal is received by the transducer elements where the time of arrival at each sensor depends on the position of the scatterer and the array geometry. The signal received by the central element is denoted by

$$f(t) = h(t)e^{j\frac{2\pi}{\lambda}ct} \tag{2}$$

where $h(t)$ is the signal envelope, and λ is the center wavelength of the transducer. Assuming that the scatter is at the array far-field and the envelope is narrowband [71], we can express the signal, received by the element positioned at $p_{n,m}$, as

$$f_{n,m}(t) = h(t)e^{j\frac{2\pi}{\lambda}c(t-\tau_{n,m})} = f(t)e^{-j\frac{2\pi}{\lambda}c\tau_{n,m}} \tag{3}$$

where the time delay is given by

$$\tau_{n,m} = \frac{\sin\theta\left(nd_x\cos\phi + md_y\sin\phi\right)}{c}. \tag{4}$$

Beamforming is the process, in which the received signals are temporally filtered and then combined to create the final image. The conventional beamformer DAS applies appropriate delays on each of the received signals according to a certain direction of interest (θ_0, ϕ_0) and then performs a weighted sum of the results. This creates a beamformed signal given by

$$y(t) = \sum_{n=-N}^{N}\sum_{m=-M}^{M} w_R[n,m]f_{n,m}(t+\gamma_{n,m}) \tag{5}$$

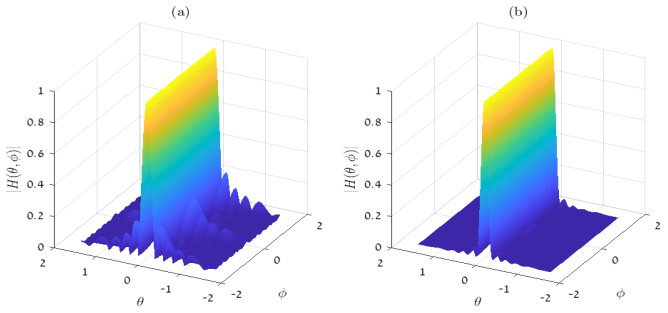

Fig. 1. Receive beam patterns. (a) DAS and (b) COBA-3D. Both beamformers use unity receive weights.

where $w_R[n,m]$ are the weights (upon reception) and the time delays are given by

$$\gamma_{n,m} = \frac{\sin\theta_0\left(nd_x\cos\phi_0 + md_y\sin\phi_0\right)}{c}. \tag{6}$$

Collecting the beamformed signals of all desired directions allows us to construct the entire 3-D image and display any required view of the scanned volume.

Assuming that the input signal is a unity amplitude plane wave $f(t) = e^{j\omega_0 t}$, where $\omega_0 = (2\pi/\lambda)c$, the expression for the receive beam pattern is given by [1]

$$\begin{aligned} H_{RX}(\theta,\phi) &\triangleq \sum_{n,m} w_R[n,m]e^{-j\tau_{n,m}} \\ &= \sum_{n,m} w_R[n,m]e^{-j\frac{2\pi}{\lambda}\sin\theta\left(nd_x\cos\phi + md_y\sin\phi\right)}. \end{aligned} \tag{7}$$

Fig. 1(a) depicts an example of a typical beam pattern created by DAS where we set $w_R[n,m] \equiv 1$. Here, we show the normalized magnitude of the beam pattern as a function of the azimuth and elevation angles where the line of sight is set to illustrate the 3-D geometry of the beam pattern.

The beam pattern can be rewritten as the 2-D spatial discrete-time Fourier transform of the aperture function $w_R[\cdot,\cdot]$

$$\begin{aligned} H_{RX}(\theta,\phi) &= \sum_{n,m} w_R[n,m]e^{-js_x n}e^{-js_y m} \\ &= \mathcal{F}_{2D}\{w_R\}(s_x, s_y) \end{aligned} \tag{8}$$

where we define the spatial frequencies

$$s_x \triangleq \frac{2\pi}{\lambda}d_x\sin\theta\cos\phi, \quad s_y \triangleq \frac{2\pi}{\lambda}d_y\sin\theta\sin\phi. \tag{9}$$

Thus, the design of the beam pattern translates to determining the aperture function.

The final image quality is also affected by the transmit beam pattern; hence, we consider the two-way beam pattern given by the pointwise product

$$H(\theta,\phi) \triangleq (H_{TX}\cdot H_{RX})(\theta,\phi). \tag{10}$$

Here, $H_{TX}(\theta,\phi)$ is the transmit beam pattern that, by the reciprocal theorem [79], can be written similar to $H_{RX}(\theta,\phi)$, where we replace $w_R[\cdot,\cdot]$ with the transmit aperture function $w_T[\cdot,\cdot]$. Thus, the two-way beam pattern can be rewritten as

$$H(\theta,\phi) = \mathcal{F}_{2D}\{w_T * w_R\}(s_x, s_y) \tag{11}$$

where $*$ represents a 2-D spatial convolution.

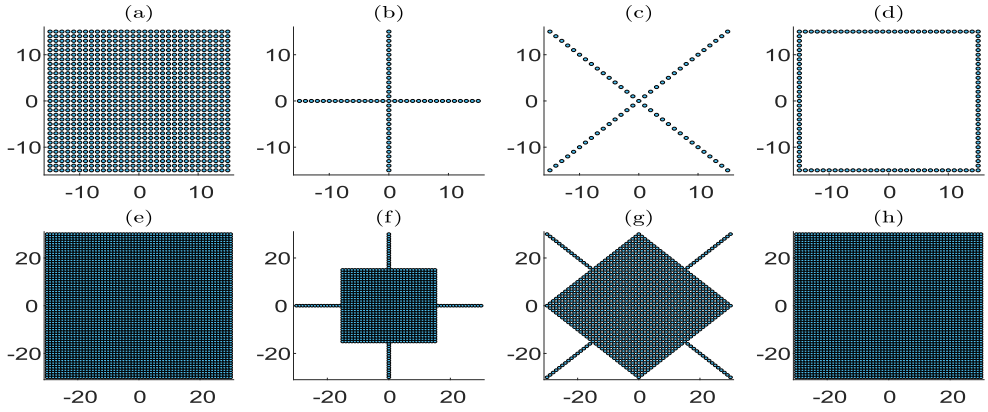

Fig. 2. Sparse arrays. (a) Original UPA—961 elements. (b) "+"-shape array—61 elements. (c) "X"-shape array—61 elements. (d) "□"-shape array—120 elements. (e)–(h) Corresponding sum coarrays with 3721, 1021, 1021, and 3721 elements, respectively. Each circle represents an array element. All sum coarrays contain within them a UPA, which, in turn, includes the original UPA.

We note that both far-field and narrowband assumptions, used in the development of (3) and (4), generally do not hold in US imaging, making the beam pattern expression theoretically invalid. However, it provides a practical tool for assessing the image resolution and contrast, governed by the main lobe and side lobes of the 2-D beam pattern [80].

B. Problem Description

The main goal of this work is to enable 3-D US imaging with reduced or limited hardware, paving the way for regular use of 3-D US in clinics worldwide. We consider the following system aspects: frame rate, image resolution, contrast, and the number of transducer elements on reception. The latter requires cumbersome receive electronics and imposes a large computational burden, which has an adverse effect on the former system aspects. Throughout this article, we assume that the center wavelength λ and the element spacing d_x and d_y are given parameters and cannot be changed. Moreover, the array aperture and possible element locations are fixed such that our task of reducing hardware translates to removing some of the elements upon reception.

We introduce a 2-D convolutional beamformer that synthetically mimics the convolution operation in (11) that occurs naturally due to the physics of the imaging system. This effectively creates a large aperture which in turn leads to improved resolution and contrast. When combined with DW transmission, our beamforming strategy enables a high frame rate, sufficient for 3-D ultrafast imaging. Furthermore, while all elements are utilized for transmission, the proposed beamformer enables the use of sparse arrays, leading to the dramatic reduction in the number of receive elements. As the construction of such thinned arrays poses another engineering challenge, we present a scalable 2-D sparse array design based on fractals. Here, we extend the design recently proposed in [72] to the 2-D setting.

III. Sparse 3-D Convolutional Beamforming

In this section, we present our main contribution: sparse beamforming techniques for ultrafast 3-D imaging. We start with a brief description of the concept of the sum coarray followed by the introduction of our 2-D convolutional beamformer. As the major computational burden arises from the receive hardware, we perform element reduction by employing 2-D sparse arrays upon reception. To complete our proposed framework, we describe a sparse array design based on fractal geometries. Note that all elements are used for transmission, implying that the transmit beam pattern remains unchanged. Therefore, as we show later, we achieve enhanced image quality by obtaining an improved receive beam pattern.

A. Preliminaries of Array Theory

We briefly present key concepts of array theory on which convolutional beamforming is based. We start with the following definition.

Definition 1: Element Set: Consider a planar array where d_x and d_y are the minimum spacing in the xy-plane of the underlying grid on which sensors are located. The *element set* is defined as an integer set E of tuples, where $(n, m) \in E$ if there is a sensor located at $(nd_x, md_y, 0)$.

For simplicity, we refer to a planar array with an element set E as a planar array E. We continue with the definition of the sum coarray.

Definition 2: Sum Coarray: Consider a planar array E. Define the sum set of E as

$$S_E = \big\{(n+u,\ m+v) : (n,m),\ (u,v) \in E\big\}. \tag{12}$$

The *sum coarray* of E is defined as the array whose element set is S_E, i.e., the planar array S_E.

As an example, the sum coarray of a UPA is another UPA, as shown in Fig. 2, of twice the size at each axis.

An additional important part of convolutional beamforming is intrinsic apodization defined in the following.

Definition 3: Intrinsic Apodization: Consider a planar array E, and define a binary indicator matrix $\mathbf{I}$ whose entries are $\mathbf{I}[n, m] = 1$ if $(n, m) \in E$ and zero otherwise. The *intrinsic apodization* of E is an integer matrix defined as

$$\mathbf{A}_E \triangleq \mathbf{I} * \mathbf{I} \tag{13}$$

where $*$ denotes 2-D convolution operation. Alternatively, the entries $a_E[n,m]$ of $\mathbf{A}_E$ can be written as

$$a_E[n,m]=\left|\left\{\Big((u,v),(k,l)\Big)\in E^2 : u+k=n, v+l=m\right\}\right|. \tag{14}$$

The sum coarray and the intrinsic apodization play important roles as they directly affect image quality. As we later demonstrate, the former dictates the size/support of the effective aperture created by COBA-3D, while the latter determines the weights of this aperture. For a more detailed discussion on the notions above, we refer the readers to [71] and references therein.

B. 3-D Convolutional Beamforming

Now, we introduce COBA-3D that extends convolutional beamforming [71] to 3-D settings with DW transmission. We include an analysis of the consequent sum coarray and receive beam pattern, leading to improved image quality. We note that, although the beamforming process is performed digitally, we use, in the following, the continuous-time notation t to simplify the presentation.

Consider imaging with a UPA E where we transmit a series of K DWs with inclination angles $\{\alpha_k,\beta_k\}_{k=0}^{K}$, and record the reflected echoes following each transmission. Upon reception, IQ sampling is first performed at a sampling rate at least as high as the Nyquist rate [40], [81] determined by the transducer center frequency. To achieve *a posteriori* synthetic transmit focusing, we coherently compound [82] the complex received signals by applying to each signal appropriate time delays depending on the element positions and the desired direction (θ_0,ϕ_0). Then, we sum (compound) the results over all transmissions to obtain the compound signal, given by

$$y_{n,m}(t)\triangleq\sum_{k=0}^{K} f_{n,m,\alpha_k,\beta_k}(t+\gamma_{n,m,\alpha_k,\beta_k}) \tag{15}$$

where f_{n,m,α_k,β_k} denotes the signal received by the element (n,m) following the transmission with inclination angles $\{\alpha_k,\beta_k\}$, and $\gamma_{n,m,\alpha_k,\beta_k}$ is the corresponding time delay (please refer to Chapter I.B of [83]). Note that the time point t in (15) is proportional to the desired axial depth z via $z=(ct/2)$.

Next, for any $n\in[-N,N]$ and $m\in[-M,M]$, we define the following signals:

$$r_{n,m}(t)\triangleq\sqrt{|y_{n,m}(t)|}\exp\{j\angle y_{n,m}(t)\} \tag{16}$$

where $|\cdot|$ and $\angle$ are the modulus and phase of the signal, respectively. Denoting by $\mathbf{r}(t)$ the matrix whose entries are $r_{n,m}(t)$, we define, for each time point, the convolution signal

$$\mathbf{c}(t)=(\mathbf{r}*\mathbf{r})(t) \tag{17}$$

where $*$ denotes 2-D spatial convolution. The matrix $\mathbf{c}(t)$ is of size $(4N+1)\times(4M+1)$ and can be computed efficiently using a spatial 2D-FFT and its inverse 2D-IFFT as

$$\mathbf{c}(t)=\text{2D-IFFT}\Big\{\text{2D-FFT}\{\mathbf{r}\}\odot\text{2D-FFT}\{\mathbf{r}\}\Big\}(t) \tag{18}$$

where $\odot$ represents the Hadamard product. The signal, beamformed at direction (θ_0,ϕ_0), is then obtained by summing all the entries of $\mathbf{c}(t)$

$$b(t)\triangleq\sum_{n=-2N}^{2N}\sum_{m=-2M}^{2M}\tilde{w}_R[n,m]\mathbf{c}_{n,m}(t) \tag{19}$$

where $\{\mathbf{c}_{n,m}(t)\}$ are the entries of $\mathbf{c}(t)$ and $\tilde{w}_R[n,m]$ are the weights (apodization) applied to the convolution signal. To attain an effective apodization of $w_R[n,m]$, the actual weights should be set as

$$\tilde{w}_R[n,m]=\frac{w_R[n,m]}{a_E[n,m]} \tag{20}$$

accounting for the intrinsic apodization $a_E[n,m]$ given by (14) that stems from the convolution operation.

The dimension (length) of the vector $b(t)$ and the number of such scan-lines are determined by the discretization along with depth (time) and the number of chosen directions (θ,ϕ), which represents the underlying grid of the reconstructed image. Finally, collecting all beamformed signals $b(t)$ of all directions allows composing the complete volumetric image defined over a predetermined 3-D grid where any region of interest within it is available for visualization.

We summarize COBA-3D in Algorithm 1. We note that here we utilize DWs; however, COBA-3D can be performed with the focused transmission or any other unfocused insonification, such as plane waves. When the focused mode is utilized, the first stage of compounding is skipped since focusing is performed upon transmission.

Algorithm 1 COBA-3D

Require: IQ signals $\{f_{n,m,\alpha,\beta}(t)\}$, weights $\{w_R[n,m]\}$.

1: Perform coherent compounding

$$y_{n,m}(t)=\sum_{k=0}^{K} f_{n,m,\alpha_k,\beta_k}(t+\gamma_{n,m,\alpha_k,\beta_k})$$

2: Compute $r_{n,m}(t)=\exp\{j\angle y_{n,m}(t)\}\sqrt{|y_{n,m}(t)|}$

3: Perform 2D convolution using 2D FFT

$$\mathbf{c}(t)=\text{IFFT}\Big\{\text{FFT}\{\mathbf{r}\}\odot\text{FFT}\{\mathbf{r}\}\Big\}(t)$$

4: Set weights $\tilde{w}_R[n,m]=\frac{w_R[n,m]}{a_E[n,m]}$

5: Calculate the beamformed signal

$$b(t)\triangleq\sum_{n=-2N}^{2N}\sum_{m=-2M}^{2M}\tilde{w}_R[n,m]\mathbf{c}_{n,m}(t)$$

Ensure: Beamformed signal $b(t)$.

In the Appendix, we analyze the receive beam pattern created by COBA-3D, leading to the following expression:

$$\begin{aligned}H_{RX}(\theta,\phi)&=\sum_{(n,m)\in S_E} w_R[n,m]e^{-j(s_x n+s_y m)}\\&=\sum_{n=-2N}^{2N}\sum_{m=-2M}^{2M} w_R[n,m]e^{-j(s_x n+s_y m)}\end{aligned} \tag{21}$$

where $w_R[\cdot,\cdot]$ are the effective receive weights. As can be seen, the receive beam pattern is directly related to the sum coarray whose aperture is larger than that of the physical array. The latter leads to a receive beam pattern with narrower main lobe and lower side lobes in comparison to DAS, as demonstrated in Fig. 1. Furthermore, for the appropriate choice of the inclination angles, coherent compounding effectively generates *a posteriori* synthetic focusing in the transmission [82], thus creating a transmit beam pattern $H_{TX}(\theta,\phi)$ that is similar to or even better than that achieved by standard focused transmissions. Thus, COBA-3D leads to an overall beam pattern of $H_{\text{COBA-3D}}(\theta,\phi) = (H_{TX} \cdot H_{RX})(\theta,\phi)$, which is superior to that created by DAS, and thus, it should theoretically result in enhanced image quality. This result is verified by practical experiments in Section IV.

The resultant algorithm, COBA-3D, resembles COBA presented in [71] but differs from that in three major aspects. First, we add a preprocessing step of compounding, which allows COBA-3D to handle unfocused transmissions and increase frame rate. COBA considers focused transmission, which limits the frame rate due to the large number of required scan-lines that can reach several tens of thousands in a 3-D setup. On the other hand, the frame rate achieved by COBA-3D is dictated by the number of inclination angles K, which is typically one order of magnitude lower than the number of scan-lines required in focused imaging, thus enabling real-time imaging. Second, COBA-3D operates on IQ signals, which removes the need to perform postbandpass or high-pass filtering. As explained in [71], when RF data are used, the spatial convolution leads to undesired low-frequency components that need to be filtered out. The latter side effect is avoided when IQ data are used, thus removing the postfiltering step of COBA. Last and most important, COBA-3D recovers volumetric data and, thus, reduces operator dependence in the imaging process. Once the 3-D data are obtained, any view of any region within it can be displayed without operating the probe, including complete views of anatomical body structures that are intrinsically 3-D, such as the mitral valve. Moreover, the volume data provide the exact location and orientation information; thus, a variety of parameters can be estimated from a 3-D image in a more accurate and reproducible fashion compared to 2-D imaging [84]–[86].

To conclude this part, COBA-3D allows handling DW transmissions, thus obtaining ultrafast frame rate. In addition, it generated an improved receive beam pattern, which potentially should lead to higher image quality than DAS. A challenge that remains is the heavy receive hardware and the corresponding sizable data that need to be processed upon reception due to a large number of receive elements.

C. Sparse Beamforming

So far, we introduced COBA-3D that is designed to achieve ultrafast frame rate and improved image resolution and contrast compared to DAS. However, still, a large number of receive elements is required, leading to high cost, power, and computational burden. Moreover, the latter increases considerably when transmitting DWs since the entire region of interest is reconstructed following each transmission (and not a single scan-line).

To obtain element reduction without degrading performance in terms of image resolution and contrast, we utilize 2-D sparse arrays defined next. This is a generalization of the sparse arrays introduced in [71] to the 2-D setting.

Definition 4: 2-D Sparse Array: Let E and T be two planar arrays, and denote by S_T the sum coarray of T. We say that T is a *sparse (or thinned) array* with respect to E if

$$T \subset E \subseteq S_T \tag{22}$$

where, in the above, we consider the elements sets of the arrays.

Suppose that we perform imaging by using a UPA E for transmitting tilted DWs where, upon reception, we employ a thinned (sparse) array T for acquiring the backscattered signals. We can no longer compute $c(t)$ as in (17) or (18) since we removed some of the elements (or signals). Therefore, we compute the convolution signal $\mathbf{c}(t)$ using pairwise multiplications of the signals as follows. Denoting by S_T the sum coarray of T, for any $(n,m) \in S_T$, we define

$$c_{n,m}(t) = \sum_{(u,v)\in T} \sum_{\substack{(k,l)\in T: \\ u+k=n \\ v+l=m}} (r_{u,v} \cdot r_{k,l})(t). \tag{23}$$

Alternatively, we can obtain (23) by filling in the missing signals with zeros and then performing a 2-D convolution

$$\mathbf{c}(t) = (\tilde{\mathbf{r}} * \tilde{\mathbf{r}})(t) \tag{24}$$

where

$$\tilde{r}_{n,m}(t) = \begin{cases} r_{n,m}(t), & (n,m) \in T \\ 0, & \text{otherwise.} \end{cases} \tag{25}$$

Finally, the beamformed signal is given by

$$b(t) = \sum_{(n,m)\in S_T} \tilde{w}_R[n,m] c_{n,m}(t) \tag{26}$$

where we incorporated the receive aperture function $\tilde{w}_R[n,m]$, determined by considering the intrinsic apodization of the sparse array T as in (20). Again, this process yields a single scan-line $b(t)$ of a specific direction and should be repeated for all desired directions to obtain the complete 3-D image. The resultant technique, referred to as sparse COBA-3D (SCOBA-3D), is outlined in Algorithm 2.

Following the same steps as in the Appendix, we can obtain an expression of the receive beam pattern created by SCOBA-3D:

$$H_{RX}(\theta,\phi) = \sum_{(n,m)\in S_T} w_R[n,m] e^{-j(s_x n + s_y m)} \tag{28}$$

where $w_R[n,m]$ is the effective apodization and $a_T[n,m]$ is the intrinsic apodization of T defined in (14). By Definition 4, we have that $E \subset S_T$; hence, we can write

$$H_{RX}(\theta,\phi) = \sum_{(n,m)\in E} w_R[n,m] e^{-j(s_x n + s_y m)} + \sum_{(n,m)\in S_T/E} w_R[n,m] e^{-j(s_x n + s_y m)} \tag{29}$$

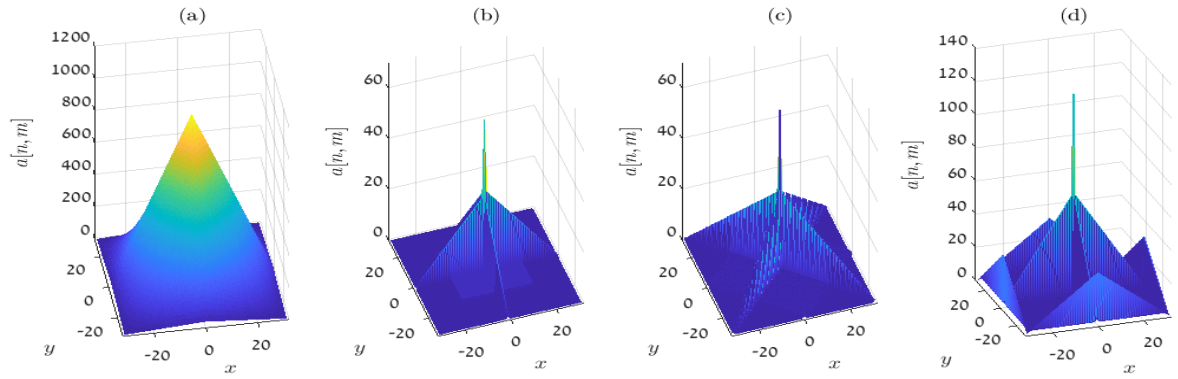

Fig. 3. Intrinsic apodization of various arrays. (a) UPA, (b) "+"-shape array, (c) "X"-shape array, and (d) "□"-shape array. Any choice of sparse array leads to different intrinsic apodization that can improve or degrade image quality. Hence, the intrinsic apodization should be considered when setting the receive weights.

Algorithm 2 SCOBA-3D

Require: IQ signals $\{f_{n,m,\alpha,\beta}(t)\}$, weights $\{w_R[n,m]\}$.

1: Perform coherent compounding

$$y_{n,m}(t) = \sum_{k=0}^{K} f_{n,m,\alpha_k,\beta_k}(t + \gamma_{n,m,\alpha_k,\beta_k})$$

2: Compute $r_{n,m}(t) = \exp\{j \angle y_{n,m}(t)\}\sqrt{|y_{n,m}(t)|}$

3: Calculate $c_{n,m}(t)$ using (23) or (24) for all $(n,m) \in S_T$

4: Set weights $\tilde{w}_R[n,m] = \frac{w_R[n,m]}{a_T[n,m]}$ for all $(n,m) \in S_T$

5: Compute the beamformed signal using (26)

$$b(t) = \sum_{(n,m)\in S_T} \tilde{w}_R[n,m] c_{n,m}(t) \tag{27}$$

Ensure: Beamformed signal $b(t)$.

where $S_T/E \triangleq \{(n,m) \in S_T : (n,m) \notin E\}$. Therefore, condition (22) ensures that the resultant sum coarray exhibits at least as large aperture as that of the fully populated array E. In the special case where we set $w_R[n,m] = 0$ for all $(n,m) \in S_T/E$, expression (28) reduces to

$$H_{RX}(\theta,\phi) = \sum_{(n,m)\in E} \hat{w}_R[n,m] e^{-j(s_x n + s_y m)} \tag{30}$$

which is the receive beam pattern achieved by DAS operating on the full array E. Hence, SCOBA-3D provides more degrees of freedom in choosing the apodization weights than DAS. Finally, since we remove elements only upon reception, the transmit beam pattern remains unchanged, as before.

Fig. 2 presents examples of various sparse arrays and their corresponding sum coarrays. All sum coarrays, in this case, include a UPA within them. A special case is the "X"-shape array whose sum coarray contains a tilted UPA. As seen, the use of sparse geometries offers a dramatic reduction in the number of elements, leading to a number of elements typically used for 2-D imaging. In addition, different sparse arrays lead to different intrinsic apodization weights, as shown in Fig. 3. Some intrinsic apodization functions can improve image quality [see Fig. 3(a)], which reduces side lobes, while others exhibit discontinuities due to zero weights that might lead to an adverse effect on the beam pattern. Therefore, any choice of receive weights has to consider the intrinsic apodization caused by the spatial convolution.

D. Fractal Array Design

Sparse arrays play a major role in convolutional beamforming. Besides the number of physical elements, there are additional important design criteria for sparse arrays that affect the performance. Examples are as follows.

Criterion 1 (Closed-Form): To allow scalability, elements locations should be given in closed-form.

Criterion 2 (Symmetric Array): Consider a planar array T, and denote by $\hat{T}$ a version of the array rotated by 180°

$$\hat{T} \triangleq \{(-n,-m) \mid (n,m) \in T\}.$$

A planar array T is symmetric if $T = \hat{T}$.

Criterion 3 (Full Sum Coarray): Consider a planar array T whose sum coarray is S_T. The sum coarray S_T is said to be *full* (i.e., contiguous) if it is a UPA. This ensures that the aperture of the sum coarray does not exhibit discontinuities, which may have an adverse effect on the beam pattern.

Criterion 4 (Large Sum Coarray): To obtain considerable element reduction, the sum coarray S_T of a sparse array T should satisfy $|S_T| = \mathcal{O}(|T|^2)$ [87]. This would lead to improved image quality since the resolution and contrast increases with sum coarray width.

Depending on the specific application, one may consider additional array properties of interest such as mutual coupling (element crosstalk) [73], but, for simplicity, we focus here on the criteria mentioned above, as we did in [73].

When considering these criteria, the design of sparse arrays becomes intractable when the number of elements is large, as in 3-D imaging. To address this issue, we adopt recent work [72], [73] and extend it to introduce a 2-D fractal array design based on the sum coarray.

Consider a planar array T whose sum coarray S_T is assumed to be full. We propose the following recursive array definition

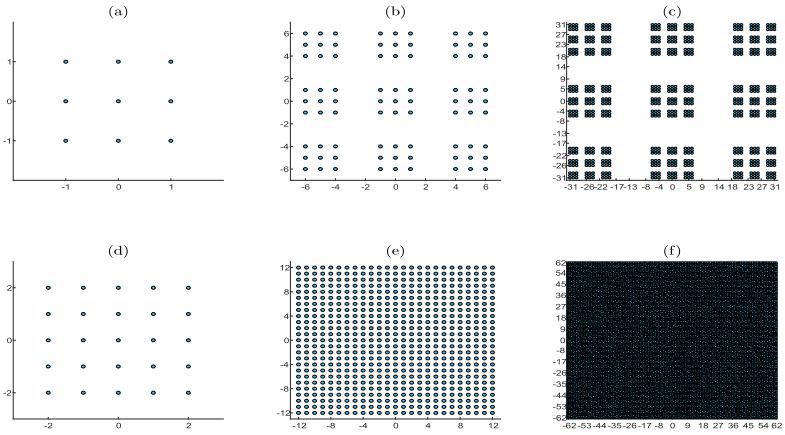

Fig. 4. Fractal arrays. (a) Generator array with nine elements and its fractal extensions. (b) F_2 and (c) F_3 with 81 and 729 elements, respectively. The corresponding sum coarrays are given in (d)–(f) with 25, 625, and 15 625 elements, respectively.

for any natural number r:

$$F_0 \triangleq \{0\},$$
$$F_{r+1} \triangleq \bigcup_{(n,m)\in T} \left(F_r + \left(n \cdot C_x^r,\, m \cdot C_y^r\right)\right) \tag{31}$$

where C_x and C_y are the number of elements in each row and column of S_T, respectively. Note that T, referred to as the generator [72], satisfies $T = F_1$. Each fractal array F_{r+1} is composed of $|T|$ replicas of F_r arranged in space according to T, leading to a total number of elements of $|T|^r$ in F_r. Fig. 4 exemplifies the proposed fractal design where we choose the generator to be a UPA.

In [72], a similar fractal array definition was proposed based on the difference coarray rather than the sum coarray as in our scheme. However, for symmetric arrays, the sum and difference coarrays are identical. Therefore, for a symmetric generator, the theoretical proofs derived in [72] apply to our case, implying that the fractal arrays inherit the properties of their generator. In particular, whenever the generator satisfies Criteria 2–4, so do its fractal expansions. Thus, the fractal scheme (31) provides a simple systematic way for designing sparse arrays by constructing a generator array with desirable properties (using, e.g., exhaustive search) and then enlarging it recursively while preserving its properties, as shown in Fig. 4.

IV. Evaluation Results

Here, we study the performance of 3-D convolutional beamforming operating on thinned receive arrays and compare it to standard DAS applied on the full array. We present experiments performed with the parallelized Verasonics systems at the University of Lyon [5], where we consider either focused transmission scheme or DW compounding. First, we present images of phantom scans and examine them to assess image resolution and contrast qualitatively and quantitatively. Then, we show results obtained from *ex vivo* data to strengthen our validation. In the following, we refer in this section for brevity to COBA-3D and SOCBA-3D as COBA and SCOBA, respectively. We begin with a full description of our experimental setup.

A. System Description

The acquisition system consists of four Vantage 256 systems (Verasonics, Kirkland, WA, USA) that are synchronized together with an external box (Verasonics, Kirkland, WA, USA). Such a configuration allows controlling 1024 individual channels in both transmission and reception. A 2-D probe is connected to the systems, each of them driving 256 elements. The probe is composed of 32×35 elements with a 300-μm pitch in both x- and y-directions (Vermon, Tours, France). We note that, in the y-direction, element lines #9, #17, and #25 are not connected [5]. For both focused and DW transmissions, a two-cycle 3-MHz sinusoidal wave is transmitted into the medium. The reception is conducted with a 12-MHz sampling frequency.

The difference between the two transmission schemes concerns the position of the focal spot, which is a positive z value in the focalized transmissions and a negative z value for DWs. For the focalized emissions, the focal spot is initially set at 40-mm depth. Then, steering is applied in both elevation (xz-plane) and azimuth (yz-plane). In both directions, the angle value is in the range $[-30°;\ 30°]$, discretized in 49 and 51 angles for elevation and azimuth directions, respectively. This leads to 2499 transmission/reception events. For DWs, the virtual focal spot is located at -4.8 mm, which is half the probe aperture. Then, steering is applied in both planes in the range $[-10°;\ 10°]$ with a discretization of nine angles in both directions, leading to a total of 81 transmission/reception events.

Throughout the experiments, we use the full aperture for transmission, whereas, upon reception, we utilize sparse arrays by removing (ignoring) part of the elements out of the full 31×31 aperture. The chosen arrays, as shown in Fig. 5, are nonfractal arrays based on nested arrays [71], [88] and were selected since they are simple to construct and their sum coarrays contain a UPA. Moreover, the different thinned configurations allow us to easily display various levels of element reduction and the effect on the size of the UPA contained in the corresponding sum coarrays. The sum coarrays lead to different beam patterns, as given in Fig. 5, leading to different

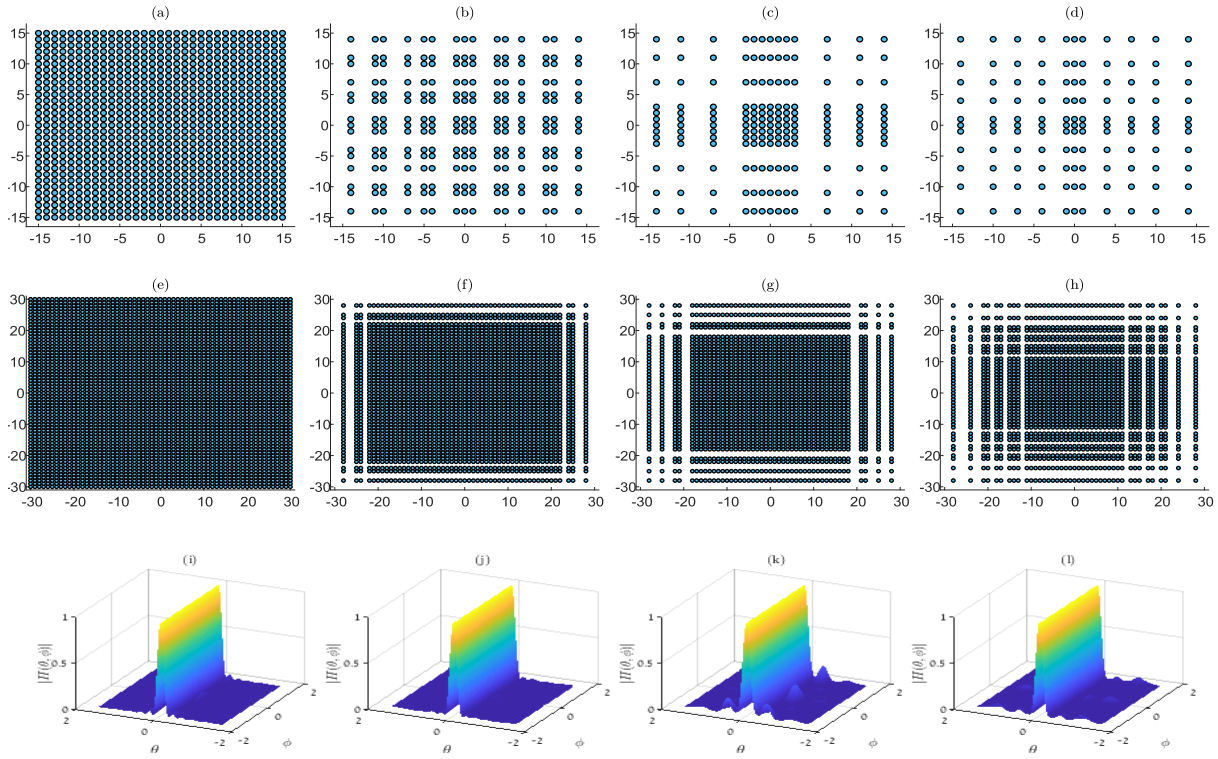

Fig. 5. Array configurations. (a) UPA with 961 elements. (b)–(d) Sparse arrays with 225, 169, and 121 elements, respectively. (e)–(h) Corresponding sum coarrays and (i)–(l) respective beam patterns, exhibited by SCOBA .

image qualities as we later demonstrate in this section. For clarity, the sparse arrays [see Fig. 5(b)–(d)] are denoted as arrays I–III, respectively. We apply DAS and COBA on the UPA of Fig. 5 and SCOBA on arrays I–III where we refer to the resultant methods as SCOBA I–III accordingly. In addition, no apodization is applied in any of the methods examined for a fair comparison.

The proposed fractal design aims at constructing a large sparse array. Here, due to our available system setup, we are confined to a 31×31 aperture that is considered to be small for our purposes, thus limiting us in showing the full extent of our recursive array scheme. However, for completeness of our work, we provide additional results obtained using the sparse fractal array in Fig. 4(b), which consists of 81 out of 169 (13×13) elements comprising the full counterpart array. Note that this fractal array satisfies Criteria 1–3 but not criterion 4 since its generator fails to meet it, as seen from Fig. 4(a) and (d). As a proper comparison, we present results obtained with DAS operating on the full 13×13 array with either focused or DW transmission.

B. Phantom Experiments

First, both transmission schemes are used on a commercial grayscale phantom (Gammex Sono410 model). We start with the focused transmission. Fig. 6 provides various images obtained by the different beamforming techniques. The images include an anechoic cyst which is used to visually assess the contrast of the recovered images. Examining the cyst, we can see that COBA generates sharper images than DAS. SCOBA

TABLE I
CR [dB]. THE NUMBERS IN BRACKETS DENOTE THE NUMBER OF RECEIVE ELEMENTS

	DAS (961)	COBA (961)	SCOBA I (225)	SCOBA II (169)	SCOBA III (121)
Focused	-23.97	-30.60	-30.57	**-30.71**	-27.86
DW	-7.38	**-10.20**	-9.70	-8.69	-6.52

achieves similar or improved contrast in comparison to DAS while offering fourfold to eightfold element reductions upon reception. A closer look at the performance of the beamformer is shown in Fig. 7, where we display cross sections of the cyst to visually assess contrast. As a quantitative measure, we compute the contrast ratio (CR) [89]

$$\mathrm{CR} = 20 \log_{10}\left(\frac{\mu_{\mathrm{cyst}}}{\mu_{bck}}\right) \tag{32}$$

where μ_{cyst} and μ_{bck} are the mean image intensities, prior to log-compression, computed over two regions inside the cyst and in the surrounding background, respectively. The chosen regions are marked by red dashed circles in Fig. 7. The results, as given in Table I, show that COBA exhibits enhanced image contrast and SCOBA variants compared to DAS. In addition, we compute the generalized contrast-to-noise ratio (gCNR) [90], which is robust against dynamic range alterations. The results, as shown in Table II, are consistent with our previous findings and provide additional validation of the proposed methods.

Now, we study the resolution of the obtained images. To that end, we use phantom images that comprise point

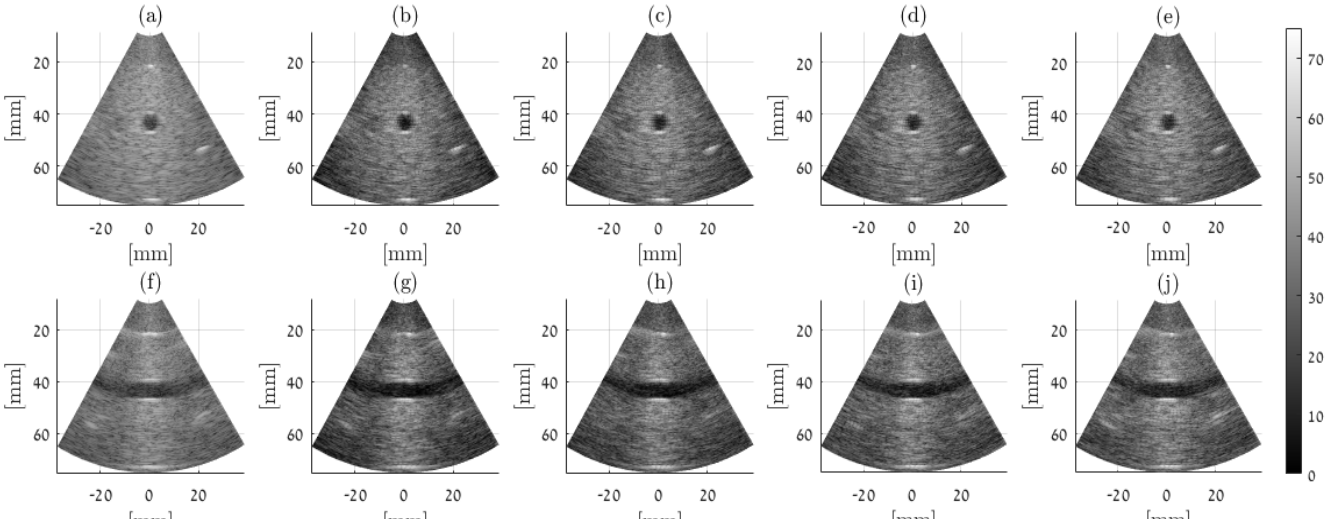

Fig. 6. Orthogonal views of (a)–(e) *xz* and (f)–(j) *yz* planes of a Gammex phantom with anechoic cyst obtained using focused transmission with DAS (961), COBA (961), SCOBA I (225), SCOBA II (169), and SCOBA III (121) in their respective order from left to right. Numbers in brackets refer to the number of receive elements.

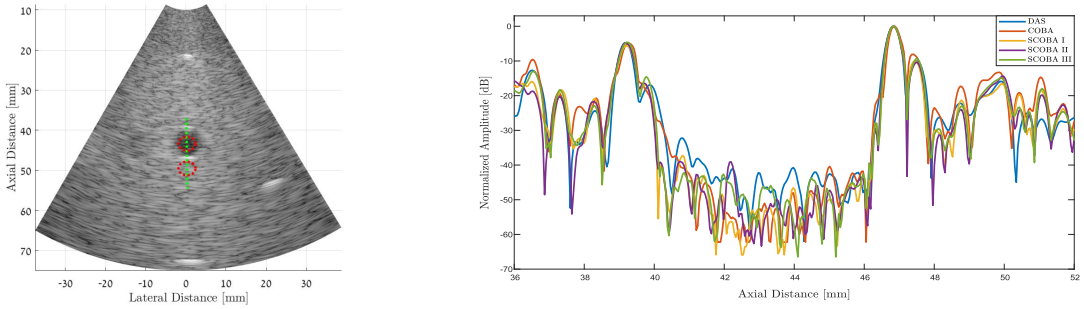

(a) (b)

Fig. 7. (a) Red circles mark the areas used for computing the CR values of Table I, while green dashed line indicates the location of the cross section shown in (b) to evaluate contrast.

TABLE II
gCNR. THE NUMBERS IN BRACKETS DENOTE THE NUMBER OF RECEIVE ELEMENTS

	DAS (961)	COBA (961)	SCOBA I (225)	SCOBA II (169)	SCOBA III (121)
Focused	0.777	0.871	0.871	**0.873**	0.838
DW	0.303	**0.408**	0.390	0.353	0.269

TABLE III
FWHM [mm]. THE NUMBERS IN BRACKETS DENOTE THE NUMBER OF RECEIVE ELEMENTS

	DAS (961)	COBA (961)	SCOBA I (225)	SCOBA II (169)	SCOBA III (121)
Focused	1.89	**0.94**	**0.94**	**0.94**	**0.94**
DW	2.65	**1.36**	1.68	1.76	1.84

targets. Examining the results in Fig. 8, specifically the points scatterers, we can see that COBA and SCOBA variants provide improved resolution compared to DAS. This is the result that strengthens when the cross section of a chosen point scatterer is displayed in Fig. 9, showing that the variants of SCOBA yield better resolution than DAS, and COBA outperforms them all. In addition, we compute the full-width at half-maximum (FWHM) to quantitatively measure the resolution obtained by each method. The results are given in Table III, emphasizing the enhanced resolution offered by the proposed beamforming algorithms.

Next, we examine the proposed techniques when DW transmission is used to achieve a high frame rate. In Fig. 10, we present images of the anechoic cyst, acquired with unfocused insonification and recovered by performing coherent compounding upon reception. These results along with the cross sections shown in Fig. 11 prove that the proposed techniques are suitable for DW transmission. COBA clearly demonstrates better contrast than DAS, while all variants of SCOBA outperform DAS in terms of contrast where their performance increases with the number of elements. The CR and gCNR values given in Tables I and II, respectively, verify these conclusions.

To estimate image resolution, we show additional images in Fig. 12, which includes point targets. The cross section presented in Fig. 13 displays the resolution improvement obtained by COBA and the selected versions of SCOBA. These results are supported quantitatively by the FWHM values in Table III.

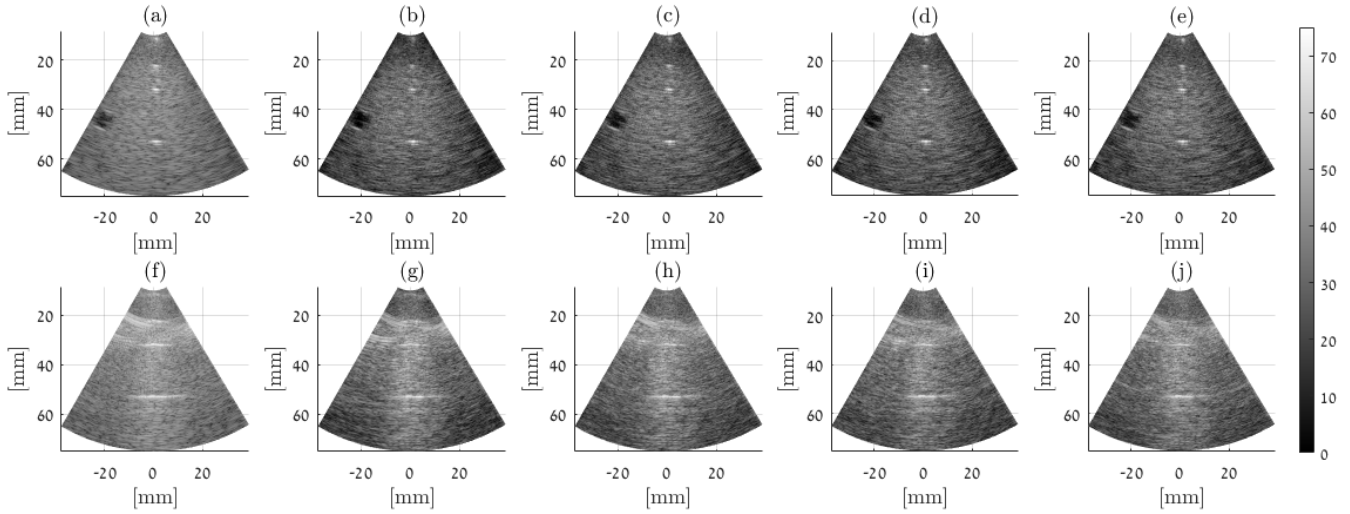

Fig. 8. Orthogonal views of (a)–(e) *xz* and (f)–(j) *yz* planes of a Gammex phantom with punctual targets obtained using focused transmission with (a) DAS (961), (b) COBA (961), and (c) SCOBA I (225), SCOBA II (169), and SCOBA III (121). Numbers in brackets refer to the number of receive elements.

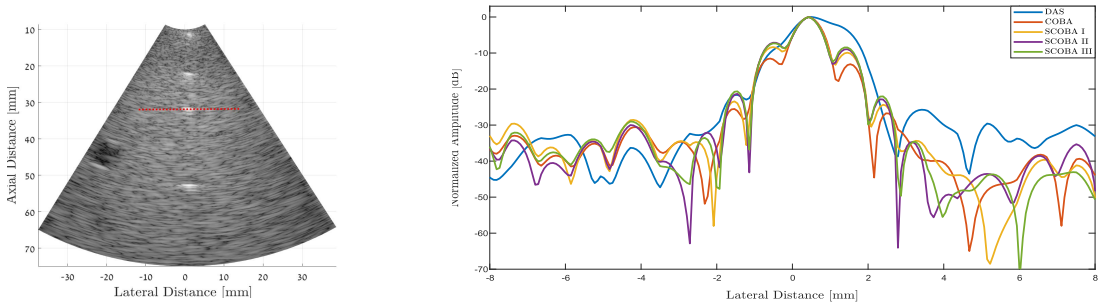

(a) (b)

Fig. 9. (a) Red dashed line marks the location of the cross section shown in (b) to assess resolution.

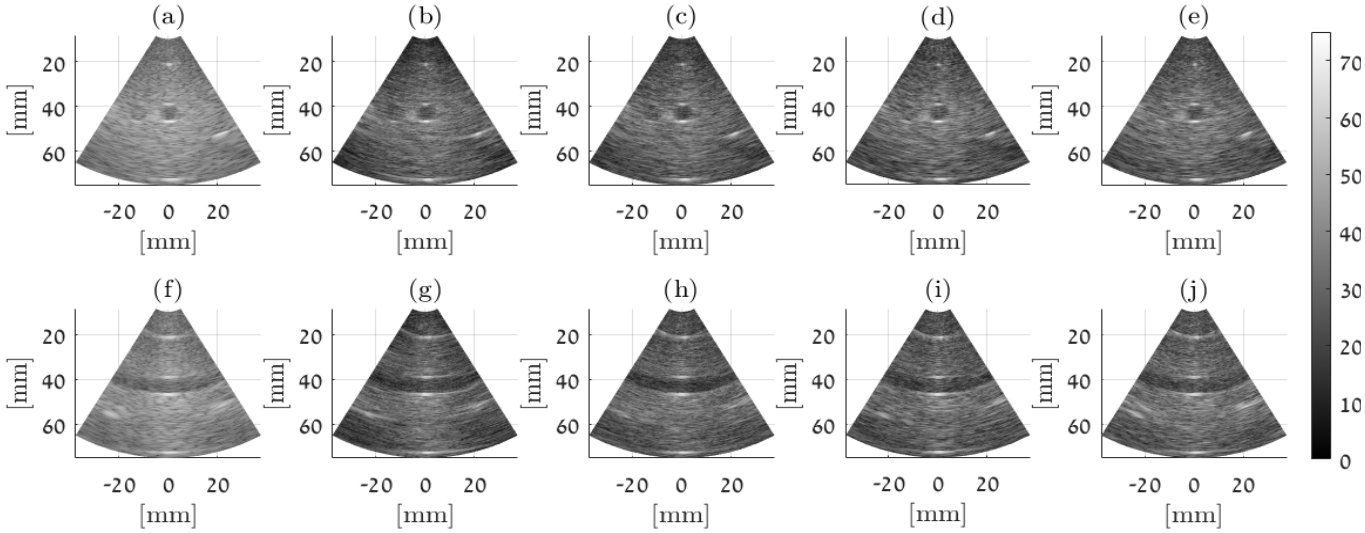

Fig. 10. Orthogonal views of (a)–(e) *xz* and (f)–(j) *yz* planes of a Gammex phantom with anechoic cyst obtained using DWs with DAS (961), COBA (961), SCOBA I (225), SCOBA II (169), and SCOBA III (121) in their respective order from left to right. Numbers in brackets refer to the number of receive elements.

We complete this part by demonstrating the use of our recursive scheme where we expand a nine element UPA to create the fractal array F_2 shown in Fig. 4(b). The fractal sparse array is utilized to perform 3-D imaging with either focused transmission or DW compounding where we apply SCOBA upon reception. Fig. 14 displays resultant images and

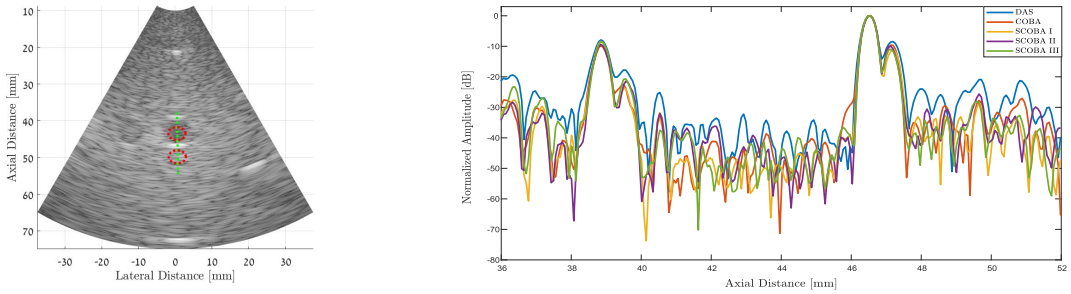

(a) (b)

Fig. 11. (a) Red circles point to the areas used for computing the CR values of Table I, while green dashed line marks the location of the cross section shown in (b) to assess contrast.

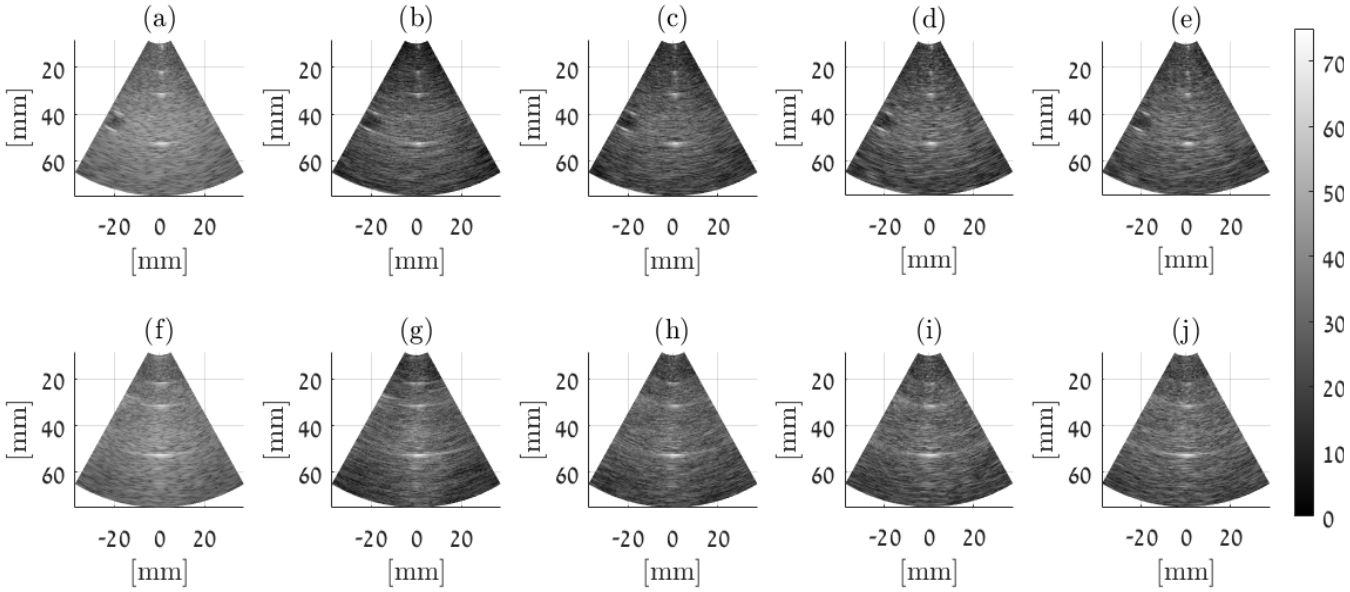

Fig. 12. Orthogonal views of (a)–(e) *xz* and (f)–(j) *yz* planes of a Gammex phantom with punctual targets obtained using DWs with DAS (961), COBA (961), SCOBA I (225), SCOBA II (169), and SCOBA III (121) in their respective order from left to right. Numbers in brackets refer to the number of receive elements.

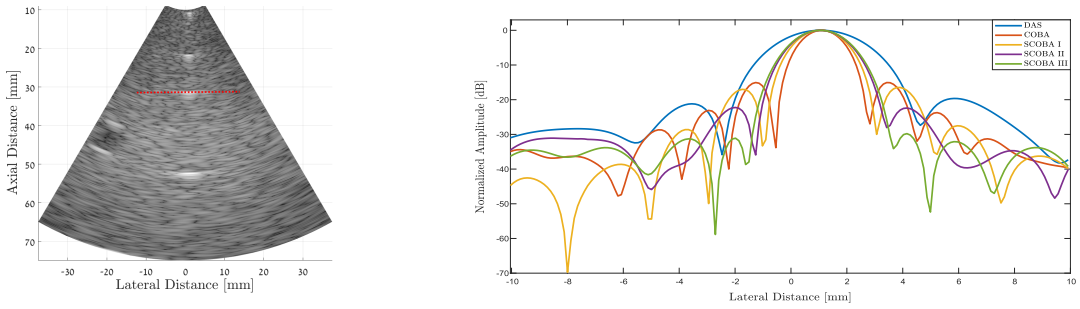

(a) (b)

Fig. 13. (a) Red dashed line indicates the location of the cross section shown in (b) to assess resolution.

images recovered by DAS operating on a 13×13 element array (full receive aperture). Assessing the images visually, one can see that the use of the fractal array led to images that exhibit better resolution and contrast compared to those created by DAS while utilizing fewer than half of the receive elements (81 out of 169). These results show the simplicity and efficiency of the proposed fractal design and in performing sparse beamforming.

We note that the images of Fig. 14 are of low quality compared to the previous results, which is expected, since here we use a considerably smaller aperture upon reception. However, we emphasize that the goal of showing these results is to exemplify the use of fractal arrays, rather than presenting improved beamforming performance.

C. Ex Vivo Experiments

Finally, *ex vivo* acquisitions were performed, scanning a lamb kidney. This medium has a typical external shape, and it also exhibits, in its internal structure, characteristics that

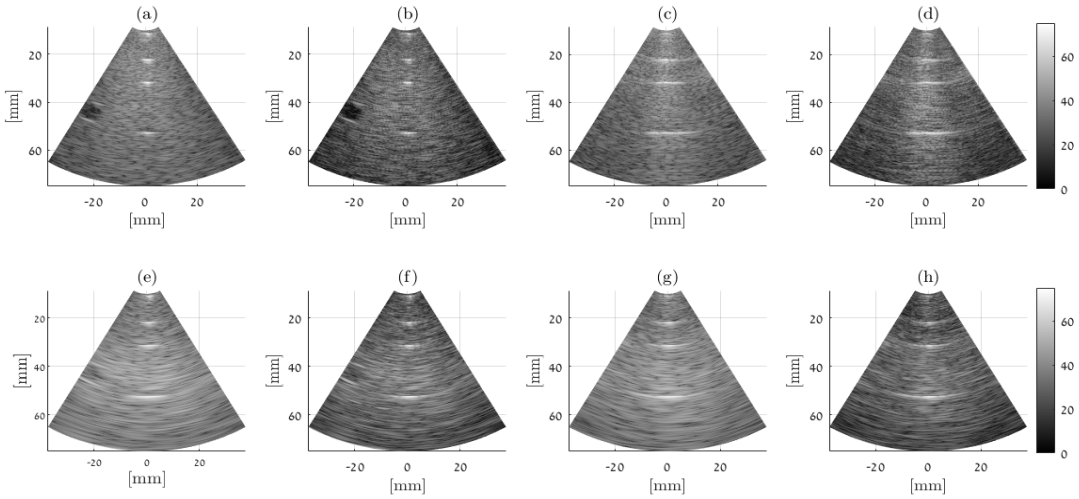

Fig. 14. Images of the *xz* (left) and *yz* (right) plane of a Gammex phantom acquired using a 161 (13 × 13) element UPA with either (a)–(d) focused transmission or (e)–(h) DWs. Upon reception, we applied DAS on the full receive array to (a), (c), (e), and (g) produce images. (b), (d), (f), and (h) Other images were obtained by SCOBA operating on an 81-element fractal receive array shown in Fig. 4(b).

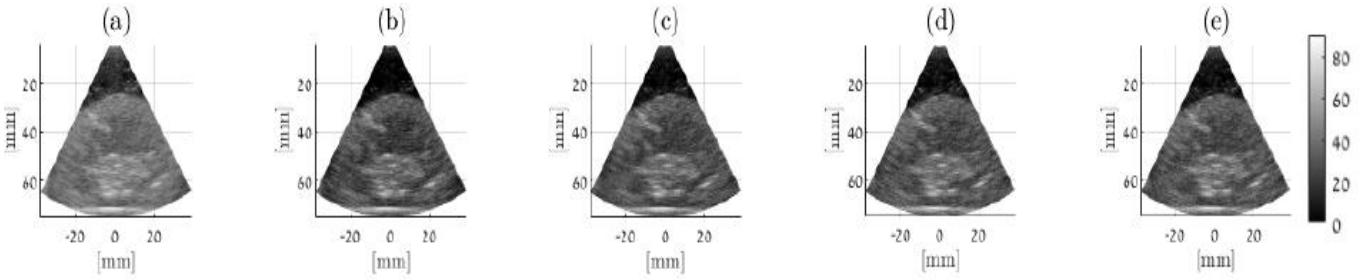

Fig. 15. Images of the *xz* plane of a lamb kidney using focused transmission with (a) DAS (961), (b) COBA (961), (c) SCOBA I (225), (d) SCOBA II (169), and (e) SCOBA III (121) in their respective order from left to right. Numbers in brackets refer to the number of receive elements.

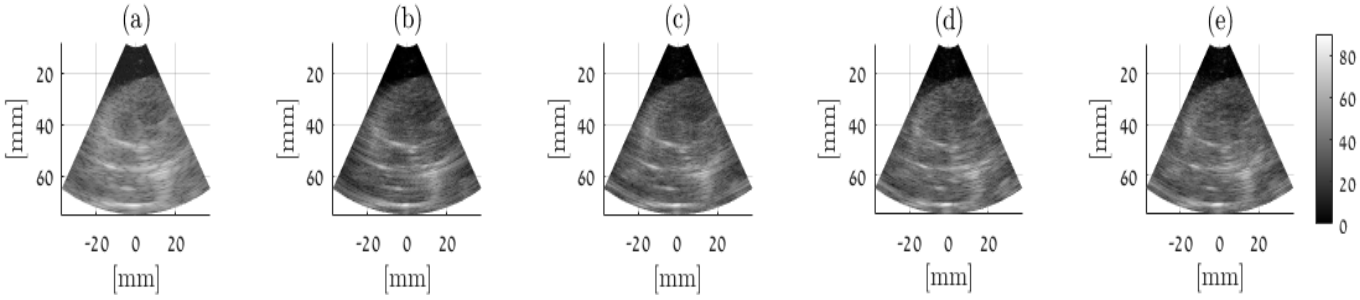

Fig. 16. Images of the *xz*-plane of a lamb kidney obtained using DWs with (a) DAS (961), (b) COBA (961), (c) SCOBA I (225), (d) SCOBA II (169), and (e) SCOBA III (121) in their respective order from left to right. Numbers in brackets refer to the number of receive elements.

should be found in 3-D US imaging (e.g., vascularization). To properly assess the proposed beamforming strategy for *ex vivo* acquisitions, we maintain the same transmission/reception settings as before. Given the size of the imaged tissues, the probe has been placed in order to scan the larger possible section of each medium. Fig. 15 presents various results acquired using focused transmission, while Fig. 16 displays images obtained with DW compounding. It can be seen from the results that COBA and SCOBA yield images with higher contrast than DAS. Examining the images of Fig. 16, we can clearly observe the improvement in resolution achieved by COBA and SCOBA. Thus, these images provide strong evidence that the proposed techniques outperform DAS. SCOBA variants offer similar or better image quality than DAS while allowing fourfold to eightfold element reductions, thus enabling high-quality 3-D US imaging.

We end the experiments with the last results obtained using the fractal array of Fig. 4(b). The generated images are shown in Fig. 17 in comparing to DAS as before. These results show the applicability of our recursive array design with SCOBA, leading to improved performance, superior to DAS,

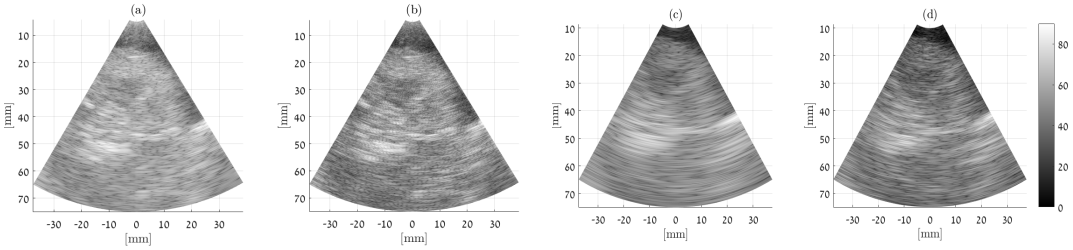

Fig. 17. Images of the *xz*-plane of a lamb kidney. (a) and (c) Images obtained by DAS operating on a 161 (13 × 13)-element receive UPA with focused and DW transmission, respectively. (b) and (d) Images obtained by SCOBA operating on an 81-element fractal receive array [see Fig. 4b] with focused and DW transmission, respectively.

where we use significantly fewer elements than DAS without compromising image quality.

V. Conclusion

In this work, we introduced COBA-3D that extends the notion of convolutional beamforming to the 3-D setting with unfocused insonification. The key part of COBA-3D is the 2-D spatial convolution of the received signals, computed efficiently in the Fourier domain. This results in improved image resolution and contrast in comparison to DAS. We relate this improvement in image quality to the virtual sum coarray, which is larger than the physical array and, thus, yields an enhanced receive beam pattern. Furthermore, we presented SCOBA-3D that exploits sparse arrays whose sum coarrays are large to perform 3-D imaging with notable fourfold to eightfold element reductions upon reception. To complete our approach, we introduced a fractal design that expands recursively a generator array with favorable properties to create an arbitrarily large sparse array with the same properties. This design facilitates the construction of sparse arrays with multiple desired properties, and its impact should increase as technology advances and the number of elements grows.

To assess the performance of our proposed techniques, we performed various experiments on phantom scans, including focused and DW transmissions. The qualitative and quantitative results verify that COBA-3D achieves improved image resolution and contrast in comparison to DAS. In addition, SCOBA-3D enables to generate high-quality 3-D images with a small number of receive elements, typically found in 1-D probes. Similar results were obtained in *ex-vivo* experiments, validating the proposed methods.

To summarize, convolutional beamforming for 3-D imaging offers enhanced image quality in terms of both resolution and contrast. Moreover, it can be easily combined with unfocused insonification, such as DW compounding, to allow an ultrafast frame rate. Finally, our fractal array design complements the proposed beamforming by allowing us to construct sparse arrays where the majority of receive electronics are discarded. Thus, we reduce the processing rate, cost, and power, facilitating the use of high-performance 3-D US imaging with limited hardware.

Appendix
Receive Beam Pattern Analysis

Here, we derive an expression of the receive 2-D beam pattern created by COBA-3D. The following can be seen as an extension to 2-D of the beam pattern analysis given in [71].

Assume that the input signal is $f(t) = e^{j\omega_0 t}$ impinging on the array at some direction (θ_0, ϕ_0). Thus, we obtain

$$r_{n,m}(t) = e^{j\omega_0 t} e^{-j\omega_0 \tau_{n,m}} \tag{33}$$

where $\tau_{n,m}$ is defined in (4). The beamformed signal can be expressed as

$$b(t) = \sum_{(u,v)\in E} \sum_{(k,l)\in E} (r_{u,v} \cdot r_{k,l})(t). \tag{34}$$

Notice that

$$(r_{u,v} \cdot r_{k,l})(t) = e^{j\omega_0 t} r_{u+k,v+l}(t). \tag{35}$$

Therefore, we get

$$b(t) = \sum_{(n,m)\in S_E} \tilde{w}_R[n,m] a_E[n,m] e^{j\omega_0 t} r_{n,m}(t) \tag{36}$$

where $\tilde{w}_R[n,m]$ is the receive apodization weights, S_E is the sum coarray of E, and $a_E[n,m]$ is the corresponding intrinsic apodization given by (14). Substituting (33) into (36), we obtain

$$b(t) = e^{j2\omega_0 t} \sum_{(n,m)\in S_E} w_R[n,m] e^{-j\omega_0 \tau_{n,m}} \tag{37}$$

where we define $w_R[n,m] \triangleq \tilde{w}_R[n,m] a_E[n,m]$. Notice that the weights $\tilde{w}_R[n,m]$ should consider the intrinsic apodization to obtain a desired effective apodization $w_R[n,m]$.

Consequently, the receive beam pattern of COBA-3D is

$$H_{\text{COBA-3D}}(\theta,\phi) = \sum_{(n,m)\in S_E} w_R[n,m] e^{-j(s_x n + s_y m)} \tag{38}$$

where s_x and s_y are given by (9). The resultant beam pattern depends on the sum coarray and the intrinsic apodization. When the physical array E is a UPA, then S_E is another UPA of twice the aperture size in both axes. A larger aperture implies better image resolution. Moreover, it increases the degrees of freedom in determining the apodization. Hence, an appropriate choice of the weights, which accounts for the intrinsic apodization, can lead to effective weights, such as Hamming apodization, which enhances the image contrast.

Acknowledgment

The RF Verasonics generator was cofounded by the FEDER program, Saint-Etienne Metropole (SME), and Conseil General de la Loire (CG42) within the framework of the SonoCardio-Protection Project led by Pr Pierre Croisille. The authors would like to thank LabTAU for their contribution in

the development of the 32 × 32 probe prototype compatible with driving by 1-to-4 Verasonics Vantage 256 and for the provision of two Vantage 256 systems.

REFERENCES

[1] A. Fenster and J. C. Lacefield, *Ultrasound Imaging and Therapy*. Oxfordshire, U.K.: Taylor & Francis, 2015.

[2] K. E. Thomenius, "Evolution of ultrasound beamformers," in *Proc. IEEE Ultrason. Symp.*, Nov. 1996, pp. 1615–1622.

[3] M. Karaman, P.-C. Li, and M. O'Donnell, "Synthetic aperture imaging for small scale systems," *IEEE Trans. Ultrason., Ferroelectr., Freq. Control*, vol. 42, no. 3, pp. 429–442, May 1995.

[4] A. Eklund, P. Dufort, D. Forsberg, and S. M. LaConte, "Medical image processing on the GPU—Past, present and future," *Med. Image Anal.*, vol. 17, no. 8, pp. 1073–1094, Dec. 2013.

[5] L. Petrusca *et al.*, "Fast volumetric ultrasound B-mode and Doppler imaging with a new high-channels density platform for advanced 4D cardiac imaging/therapy," *Appl. Sci.*, vol. 8, no. 2, p. 200, Jan. 2018.

[6] J. A. Jensen *et al.*, "SARUS: A synthetic aperture real-time ultrasound system," *IEEE Trans. Ultrason., Ferroelectr., Freq. Control*, vol. 60, no. 9, pp. 1838–1852, Sep. 2013.

[7] J. Provost, C. Papadacci, C. Demene, J.-L. Gennisson, M. Tanter, and M. Pernot, "3-D ultrafast Doppler imaging applied to the noninvasive mapping of blood vessels *in vivo*," *IEEE Trans. Ultrason., Ferroelectr., Freq. Control*, vol. 62, no. 8, pp. 1467–1472, Aug. 2015.

[8] B. Savord and R. Solomon, "Fully sampled matrix transducer for real time 3D ultrasonic imaging," in *Proc. IEEE Symp. Ultrason.*, Oct. 2003, pp. 945–953.

[9] D. Wildes *et al.*, "4-D ICE: A 2-D array transducer with integrated ASIC in a 10-fr catheter for real-time 3-D intracardiac echocardiography," *IEEE Trans. Ultrason., Ferroelectr., Freq. Control*, vol. 63, no. 12, pp. 2159–2173, Dec. 2016.

[10] P. Santos, G. U. Haugen, L. Løvstakken, E. Samset, and J. D'hooge, "Diverging wave volumetric imaging using subaperture beamforming," *IEEE Trans. Ultrason., Ferroelectr., Freq. Control*, vol. 63, no. 12, pp. 2114–2124, Dec. 2016.

[11] G. Matrone, A. S. Savoia, M. Terenzi, G. Caliano, F. Quaglia, and G. Magenes, "A volumetric CMUT-based ultrasound imaging system simulator with integrated reception and μ-beamforming electronics models," *IEEE Trans. Ultrason., Ferroelectr., Freq. Control*, vol. 61, no. 5, pp. 792–804, May 2014.

[12] A. Bhuyan *et al.*, "Integrated circuits for volumetric ultrasound imaging with 2-D CMUT arrays," *IEEE Trans. Biomed. Circuits Syst.*, vol. 7, no. 6, pp. 796–804, Dec. 2013.

[13] J. Kortbek, J. A. Jensen, and K. L. Gammelmark, "Sequential beamforming for synthetic aperture imaging," *Ultrasonics*, vol. 53, no. 1, pp. 1–16, Jan. 2013.

[14] R. Fisher *et al.*, "Reconfigurable arrays for portable ultrasound," in *Proc. IEEE Ultrason. Symp.*, Sep. 2005, pp. 495–499.

[15] I. O. Wygant *et al.*, "An integrated circuit with transmit beamforming flip-chip bonded to a 2-D CMUT array for 3-D ultrasound imaging," *IEEE Trans. Ultrason., Ferroelectr., Freq. Control*, vol. 56, no. 10, pp. 2145–2156, Oct. 2009.

[16] S. W. Smith, H. G. Pavy, and O. T. von Ramm, "High-speed ultrasound volumetric imaging system. I. Transducer design and beam steering," *IEEE Trans. Ultrason., Ferroelectr., Freq. Control*, vol. 38, no. 2, pp. 100–108, Mar. 1991.

[17] O. T. von Ramm, S. W. Smith, and H. G. Pavy, "High-speed ultrasound volumetric imaging system. II. Parallel processing and image display," *IEEE Trans. Ultrason., Ferroelectr., Freq. Control*, vol. 38, no. 2, pp. 109–115, Mar. 1991.

[18] U.-W. Lok and P.-C. Li, "Microbeamforming with error compensation," *IEEE Trans. Ultrason., Ferroelectr., Freq. Control*, vol. 65, no. 7, pp. 1153–1165, Jul. 2018.

[19] M. I. Fuller, E. V. Brush, M. D. C. Eames, T. N. Blalock, J. A. Hossack, and W. F. Walker, "The sonic window: Second generation prototype of low-cost, fully-integrated, pocket-sized medical ultrasound device," in *Proc. IEEE Ultrason. Symp.*, Sep. 2005, pp. 273–276.

[20] W. Lee, S. F. Idriss, P. D. Wolf, and S. W. Smith, "A miniaturized catheter 2-D array for real-time, 3-D intracardiac echocardiography," *IEEE Trans. Ultrason., Ferroelectr., Freq. Control*, vol. 51, no. 10, pp. 1334–1346, Oct. 2004.

[21] A. I. H. Chen, L. L. Wong, A. S. Logan, and J. T. W. Yeow, "A CMUT-based real-time volumetric ultrasound imaging system with row-column addressing," in *Proc. IEEE Int. Ultrason. Symp.*, Oct. 2011, pp. 1755–1758.

[22] M. F. Rasmussen and J. A. Jensen, "3D ultrasound imaging performance of a row-column addressed 2D array transducer: A simulation study," *Proc. SPIE*, vol. 8675, Mar. 2013, Art. no. 86750C.

[23] M. F. Rasmussen and J. A. Jensen, "3-D ultrasound imaging performance of a row-column addressed 2-D array transducer: A measurement study," in *Proc. IEEE Int. Ultrason. Symp. (IUS)*, Jul. 2013, pp. 1460–1463.

[24] M. F. Rasmussen, T. L. Christiansen, E. V. Thomsen, and J. A. Jensen, "3-D imaging using row-column-addressed arrays with integrated apodization—Part I: Apodization design and line element beamforming," *IEEE Trans. Ultrason., Ferroelectr., Freq. Control*, vol. 62, no. 5, pp. 947–958, May 2015.

[25] T. L. Christiansen, M. F. Rasmussen, J. P. Bagge, L. N. Moesner, J. A. Jensen, and E. V. Thomsen, "3-D imaging using row–column-addressed arrays with integrated apodization—Part II: Transducer fabrication and experimental results," *IEEE Trans. Ultrason., Ferroelectr., Freq. Control*, vol. 62, no. 5, pp. 959–971, May 2015.

[26] I. Ben Daya, A. I. H. Chen, M. J. Shafiee, A. Wong, and J. T. W. Yeow, "Compensated row-column ultrasound imaging system using multilayered edge guided stochastically fully connected random fields," *Sci. Rep.*, vol. 7, no. 1, Dec. 2017, Art. no. 10644.

[27] H. Bouzari *et al.*, "Curvilinear 3-D imaging using row-column-addressed 2-D arrays with a diverging lens: Feasibility study," *IEEE Trans. Ultrason., Ferroelectr., Freq. Control*, vol. 64, no. 6, pp. 978–988, Jun. 2017.

[28] M. Flesch *et al.*, "4D *in vivo* ultrafast ultrasound imaging using a row-column addressed matrix and coherently-compounded orthogonal plane waves," *Phys. Med. Biol.*, vol. 62, no. 11, p. 4571, 2017.

[29] A. S. Logan, L. L. P. Wong, A. I. H. Chen, and J. T. W. Yeow, "A 32 × 32 element row-column addressed capacitive micromachined ultrasonic transducer," *IEEE Trans. Ultrason., Ferroelectr., Freq. Control*, vol. 58, no. 6, pp. 1266–1271, Jun. 2011.

[30] A. Savoia *et al.*, "P2B-4 crisscross 2D cMUT array: Beamforming strategy and synthetic 3D imaging results," in *Proc. IEEE Ultrason. Symp.*, Oct. 2007, pp. 1514–1517.

[31] M. Yang, R. Sampson, S. Wei, T. F. Wenisch, and C. Chakrabarti, "Separable beamforming for 3-D medical ultrasound imaging," *IEEE Trans. Signal Process.*, vol. 63, no. 2, pp. 279–290, Jan. 2015.

[32] K. Owen, M. I. Fuller, and J. A. Hossack, "Application of X-Y separable 2-D array beamforming for increased frame rate and energy efficiency in handheld devices," *IEEE Trans. Ultrason., Ferroelectr., Freq. Control*, vol. 59, no. 7, pp. 1332–1343, Jul. 2012.

[33] S. I. Nikolov and J. A. Jensen, "Investigation of the feasibility of 3D synthetic aperture imaging," in *Proc. IEEE Symp. Ultrason.*, Oct. 2003, pp. 1903–1906.

[34] J. A. Jensen, S. I. Nikolov, K. L. Gammelmark, and M. H. Pedersen, "Synthetic aperture ultrasound imaging," *Ultrasonics*, vol. 44, pp. e5–e15, Dec. 2006.

[35] J. Kortbek, J. A. Jensen, and K. L. Gammelmark, "Synthetic aperture sequential beamforming," in *Proc. IEEE Ultrason. Symp.*, Nov. 2008, pp. 966–969.

[36] I. O. Wygant, M. Karaman, O. Oralkan, and B. T. Khuri-Yakub, "Beamforming and hardware design for a multichannel front-end integrated circuit for real-time 3D catheter-based ultrasonic imaging," *Proc. SPIE*, vol. 6147, Mar. 2006, Art. no. 61470A.

[37] B. Lokesh and A. K. Thittai, "Diverging beam transmit through limited aperture: A method to reduce ultrasound system complexity and yet obtain better image quality at higher frame rates," *Ultrasonics*, vol. 91, pp. 150–160, Jan. 2019.

[38] N. Bottenus, B. C. Byram, J. J. Dahl, and G. E. Trahey, "Synthetic aperture focusing for short-lag spatial coherence imaging," *IEEE Trans. Ultrason., Ferroelectr., Freq. Control*, vol. 60, no. 9, pp. 1816–1826, Sep. 2013.

[39] Y. C. Eldar and G. Kutyniok, *Sensing: Theory and Applications*. Cambridge, U.K.: Cambridge Univ. Press, 2012.

[40] Y. C. Eldar, *Sampling Theory: Beyond Bandlimited Systems*. Cambridge, U.K.: Cambridge Univ. Press, 2015.

[41] R. Tur, Y. C. Eldar, and Z. Friedman, "Innovation rate sampling of pulse streams with application to ultrasound imaging," *IEEE Trans. Signal Process.*, vol. 59, no. 4, pp. 1827–1842, Apr. 2011.

[42] X. Zhuang, Y. Zhao, Z. Dai, H. Wang, and L. Wang, "Ultrasonic signal compressive detection with sub-Nyquist sampling rate," *J. Sci. Ind. Res.*, vol. 71, pp. 195–199, Mar. 2012.

[43] J. Zhou, Y. He, M. Chirala, B. M. Sadler, and S. Hoyos, "Compressed digital beamformer with asynchronous sampling for ultrasound imaging," in *Proc. IEEE Int. Conf. Acoust., Speech Signal Process.*, May 2013, pp. 1056–1060.

[44] H. Liebgott, R. Prost, and D. Friboulet, "Pre-beamformed RF signal reconstruction in medical ultrasound using compressive sensing," *Ultrasonics*, vol. 53, no. 2, pp. 525–533, Feb. 2013.

[45] A. Achim, B. Buxton, G. Tzagkarakis, and P. Tsakalides, "Compressive sensing for ultrasound RF echoes using a-stable distributions," in *Proc. Annu. Int. Conf. IEEE Eng. Med. Biol.*, Aug. 2010, pp. 4304–4307.

[46] G. Tzagkarakis, A. Achim, P. Tsakalides, and J.-L. Starck, "Joint reconstruction of compressively sensed ultrasound RF echoes by exploiting temporal correlations," in *Proc. IEEE 10th Int. Symp. Biomed. Imag.*, Apr. 2013, pp. 632–635.

[47] C. Quinsac, A. Basarab, and D. Kouamé, "Frequency domain compressive sampling for ultrasound imaging," *Adv. Acoust. Vibrat.*, vol. 2012, pp. 1–16, May 2012.

[48] N. Wagner, Y. C. Eldar, and Z. Friedman, "Compressed beamforming in ultrasound imaging," *IEEE Trans. Signal Process.*, vol. 60, no. 9, pp. 4643–4657, Sep. 2012.

[49] T. Chernyakova and Y. C. Eldar, "Fourier-domain beamforming: The path to compressed ultrasound imaging," *IEEE Trans. Ultrason., Ferroelectr., Freq. Control*, vol. 61, no. 8, pp. 1252–1267, Aug. 2014.

[50] K. Gedalyahu, R. Tur, and Y. C. Eldar, "Multichannel sampling of pulse streams at the rate of innovation," *IEEE Trans. Signal Process.*, vol. 59, no. 4, pp. 1491–1504, Apr. 2011.

[51] E. Baransky, G. Itzhak, N. Wagner, I. Shmuel, E. Shoshan, and Y. Eldar, "Sub-Nyquist radar prototype: Hardware and algorithm," *IEEE Trans. Aerosp. Electron. Syst.*, vol. 50, no. 2, pp. 809–822, Apr. 2014.

[52] T. Chernyakova *et al.*, "Fourier-domain beamforming and structure-based reconstruction for plane-wave imaging," *IEEE Trans. Ultrason., Ferroelectr., Freq. Control*, vol. 65, no. 10, pp. 1810–1821, Oct. 2018.

[53] A. Burshtein, M. Birk, T. Chernyakova, A. Eilam, A. Kempinski, and Y. C. Eldar, "Sub-Nyquist sampling and Fourier domain beamforming in volumetric ultrasound imaging," *IEEE Trans. Ultrason., Ferroelectr., Freq. Control*, vol. 63, no. 5, pp. 703–716, May 2016.

[54] J. Liu, Q. He, and J. Luo, "A compressed sensing strategy for synthetic transmit aperture ultrasound imaging," *IEEE Trans. Med. Imag.*, vol. 36, no. 4, pp. 878–891, Apr. 2017.

[55] R. Davidsen, "Two-dimensional random arrays for real time volumetric imaging," *Ultrason. Imag.*, vol. 16, no. 3, pp. 143–163, Jul. 1994.

[56] S. S. Brunke and G. R. Lockwood, "Broad-bandwidth radiation patterns of sparse two-dimensional Vernier arrays," *IEEE Trans. Ultrason., Ferroelectr., Freq. Control*, vol. 44, no. 5, pp. 1101–1109, Sep. 1997.

[57] J. T. Yen, J. P. Steinberg, and S. W. Smith, "Sparse 2-D array design for real time rectilinear volumetric imaging," *IEEE Trans. Ultrason., Ferroelectr., Freq. Control*, vol. 47, no. 1, pp. 93–110, Jan. 2000.

[58] A. Austeng and S. Holm, "Sparse 2-D arrays for 3-D phased array imaging–design methods," *IEEE Trans. Ultrason., Ferroelectr., Freq. Control*, vol. 49, no. 8, pp. 1073–1086, Aug. 2002.

[59] M. Karaman, I. O. Wygant, O. Oralkan, and B. T. Khuri-Yakub, "Minimally redundant 2-D array designs for 3-D medical ultrasound imaging," *IEEE Trans. Med. Imag.*, vol. 28, no. 7, pp. 1051–1061, Jul. 2009.

[60] B. Diarra, M. Robini, P. Tortoli, C. Cachard, and H. Liebgott, "Design of optimal 2-D nongrid sparse arrays for medical ultrasound," *IEEE Trans. Biomed. Eng.*, vol. 60, no. 11, pp. 3093–3102, Nov. 2013.

[61] S. N. Ramadas, J. C. Jackson, J. Dziewierz, R. O'Leary, and A. Gachagan, "Application of conformal map theory for design of 2-D ultrasonic array structure for NDT imaging application: A feasibility study," *IEEE Trans. Ultrason., Ferroelectr., Freq. Control*, vol. 61, no. 3, pp. 496–504, Mar. 2014.

[62] E. Roux *et al.*, "Validation of optimal 2D sparse arrays in focused mode: Phantom experiments," in *Proc. IEEE Int. Ultrason. Symp. (IUS)*, Sep. 2017, pp. 1–4.

[63] S. K. Mitra, K. Mondal, M. K. Tchobanou, and G. J. Dolecek, "General polynomial factorization-based design of sparse periodic linear arrays," *IEEE Trans. Ultrason., Ferroelectr., Freq. Control*, vol. 57, no. 9, pp. 1952–1966, Sep. 2010.

[64] E. Roux, A. Ramalli, H. Liebgott, C. Cachard, M. C. Robini, and P. Tortoli, "Wideband 2-D array design optimization with fabrication constraints for 3-D US imaging," *IEEE Trans. Ultrason., Ferroelectr., Freq. Control*, vol. 64, no. 1, pp. 108–125, Jan. 2017.

[65] E. Roux, A. Ramalli, P. Tortoli, C. Cachard, M. C. Robini, and H. Liebgott, "2-D ultrasound sparse arrays multidepth radiation optimization using simulated annealing and spiral-array inspired energy functions," *IEEE Trans. Ultrason., Ferroelectr., Freq. Control*, vol. 63, no. 12, pp. 2138–2149, Dec. 2016.

[66] C. Tekes, M. Karaman, and F. Degertekin, "Optimizing circular ring arrays for forward-looking IVUS imaging," *IEEE Trans. Ultrason., Ferroelectr., Freq. Control*, vol. 58, no. 12, pp. 2596–2607, Dec. 2011.

[67] E. Roux, F. Varray, L. Petrusca, C. Cachard, P. Tortoli, and H. Liebgott, "Experimental 3-D ultrasound imaging with 2-D sparse arrays using focused and diverging waves," *Sci. Rep.*, vol. 8, no. 1, pp. 1–12, Dec. 2018.

[68] R. Cohen and Y. C. Eldar, "Sparse Doppler sensing based on nested arrays," *IEEE Trans. Ultrason., Ferroelectr., Freq. Control*, vol. 65, no. 12, pp. 2349–2364, Dec. 2018.

[69] R. Cohen and Y. C. Eldar, "Optimized sparse array design based on the sum coarray," in *Proc. IEEE Int. Conf. Acoust., Speech Signal Process. (ICASSP)*, Apr. 2018, pp. 3340–3343.

[70] R. Cohen and Y. C. Eldar, "Sparse emission pattern in spectral blood Doppler," in *Proc. IEEE 14th Int. Symp. Biomed. Imag. (ISBI)*, Apr. 2017, pp. 907–910.

[71] R. Cohen and Y. C. Eldar, "Sparse convolutional beamforming for ultrasound imaging," *IEEE Trans. Ultrason., Ferroelectr., Freq. Control*, vol. 65, no. 12, pp. 2390–2406, Dec. 2018.

[72] R. Cohen and Y. C. Eldar, "Sparse array design via fractal geometries," 2020, *arXiv:2001.01217*. [Online]. Available: http://arxiv.org/abs/2001.01217

[73] R. Cohen and Y. C. Eldar, "Sparse fractal array design with increased degrees of freedom," in *Proc. IEEE Int. Conf. Acoust., Speech Signal Process. (ICASSP)*, May 2019, pp. 4195–4199.

[74] C. Puente-Baliarda and R. Pous, "Fractal design of multiband and low side-lobe arrays," *IEEE Trans. Antennas Propag.*, vol. 44, no. 5, p. 730, May 1996.

[75] D. H. Werner, R. L. Haupt, and P. L. Werner, "Fractal antenna engineering: The theory and design of fractal antenna arrays," *IEEE Antennas Propag. Mag.*, vol. 41, no. 5, pp. 37–58, Oct. 1999.

[76] D. H. Wqrner and S. Ganguly, "An overview of fractal antenna engineering research," *IEEE Antennas Propag. Mag.*, vol. 45, no. 1, pp. 38–57, Feb. 2003.

[77] J. Feder, *Fractals*. Springer, 2013.

[78] K. Falconer, *Fractal Geometry: Mathematical Foundations and Applications*. 2nd ed. Hoboken, NJ, USA: Wiley, 2005.

[79] J. A. Jensen, "Ultrasound imaging and its modeling," in *Imaging of Complex Media With Acoustic and Seismic Waves*, M. Fink, W. A. Kuperman, J.-P. Montagner, and A. Tourin, Eds. Berlin, Germany: Springer, 2002, pp. 135–166.

[80] J. A. Jensen, "Linear description of ultrasound imaging systems," in *Notes for the International Summer School on Advanced Ultrasound Imaging*, vol. 5. Technical University of Denmark, 1999, p. 54.

[81] B. D. Steinberg, "Digital beamforming in ultrasound," *IEEE Trans. Ultrason., Ferroelectr., Freq. Control*, vol. 39, no. 6, pp. 716–721, Nov. 1992.

[82] G. Montaldo, M. Tanter, J. Bercoff, N. Benech, and M. Fink, "Coherent plane-wave compounding for very high frame rate ultrasonography and transient elastography," *IEEE Trans. Ultrason., Ferroelectr., Freq. Control*, vol. 56, no. 3, pp. 489–506, Mar. 2009.

[83] E. Roux, "2D sparse array optimization and operating strategy for real-time 3D ultrasound imaging," Ph.D. dissertation, Dept. Elect. Eng., Univ. Lyon, Lyon, France, 2016.

[84] R. W. Prager, U. Z. Ijaz, A. Gee, and G. M. Treece, "Three-dimensional ultrasound imaging," *Proc. Inst. Mech. Eng., H, J. Eng. Med.*, vol. 224, no. 2, pp. 193–223, 2010.

[85] K. Abo *et al.*, "Usefulness of transthoracic freehand three-dimensional echocardiography for the evaluation of mitral valve prolapse," *J. Cardiol.*, vol. 43, no. 1, pp. 17–22, 2004.

[86] J. Kwan, "Three-dimensional echocardiography: A new paradigm shift," *J. Echocardiography*, vol. 12, no. 1, pp. 1–11, Mar. 2014.

[87] R. T. Hoctor and S. A. Kassam, "The unifying role of the coarray in aperture synthesis for coherent and incoherent imaging," *Proc. IEEE*, vol. 78, no. 4, pp. 735–752, Apr. 1990.

[88] P. Pal and P. P. Vaidyanathan, "Nested arrays: A novel approach to array processing with enhanced degrees of freedom," *IEEE Trans. Signal Process.*, vol. 58, no. 8, pp. 4167–4181, Aug. 2010.

[89] M. A. Lediju, G. E. Trahey, B. C. Byram, and J. J. Dahl, "Short-lag spatial coherence of backscattered echoes: Imaging characteristics," *IEEE Trans. Ultrason., Ferroelectr., Freq. Control*, vol. 58, no. 7, pp. 1377–1388, Jul. 2011.

[90] A. Rodriguez-Molares *et al.*, "The generalized contrast-to-noise ratio: A formal definition for lesion detectability," *IEEE Trans. Ultrason., Ferroelectr., Freq. Control*, vol. 67, no. 4, pp. 745–759, Apr. 2020.